Simulation of the onset turbulent flow around a Isothermal Complex Geometries: an analysis of thermofluid dynamic flow

Rômulo D. C. Santos ⊙[a,*]**, Quétila G. Silva** ⊙[a]**, and Samia R. L. Tananta** ⊙[a]

[a] Instituto Federal de Educação, Ciência e Tecnologia do Acre (IFAC), Rio Branco - AC, Brasil

* Correspondence: lrccarvalho@gmail.com

Abstract: In this work, in the area of Computational Fluid Dynamics (CFD), more specifically in the area of thermofluid dynamics for two-dimensional flows (2D), and also considering, the fluid-body interaction, allied to the phenomena of heat-transfer by mixed convection and the beginning of processes of the turbulent flow phenomenon in the fluid-body interaction, a study is proposed that demonstrates the efficiency in the analysis and simulation of these complex phenomena. We adopt an Eulerian approach for a fixed mesh, which is intended to represent the thermofluid dynamic movement, working together with a Lagrangian mesh, the latter being intended to discretize the immersed body. The strategy, in this work, allows approaching complex isothermal geometries, which present a certain aerodynamic degree on their surface, being popularly known as blunt body, where this, in turn, is immersed in an incompressible Newtonian fluid. One of the contributions of this work is the introduction of a simple but efficient method to calculate the Nusselt number. In relation to validating and modeling the physical phenomena of interest, specifically the effectiveness of the Immersed Boundary Method, we conducted an implementation with low computational cost. This implementation was used to transfer mixed convection heat and model turbulence using the Spalart-Allmaras model within the framework of the URANS (Unsteady Reynolds Average Navier-Stokes) methodology. Numerical results showed good convergence with data available in the literature, which confirms the numerical precision and reliability of the adopted model.

Keywords: Immersed Boundary Method; Mixed Convection; Onset Turbulence; Isothermal Bluff Body.

Classification MSC: 76D05; 80A19

1 Introduction

The simulation of flows around complex geometries presents a challenging task for computational fluid dynamics. Traditional body-fitted numerical methods, which strongly couple the solution of governing equations and implementation of boundary conditions, usually need mesh generation, in general, with high computational cost. Even considering simple geometries, the generating a high quality mesh, is not a trivial job. To overcome the disadvantage of a strong coupling between the solution of governing equations and the implementation of the boundary condition in the immersed boundary, Peskin [1] presented the idea of Immersed Boundary Method (IBM) in 1971 to simulate blood flows in mitral valves of the human heart. The IBM is a numerical method that

uses Cartesian Eulerian grid points to discretize the solution of governing equations and Lagrangian points to represent the boundary of immersed body. Peskin's idea was to model the contour of the heart valve as a deformable elastic fiber with high stiffness. A small deformation or movement of the boundary would produce a force that tends to restore the boundary back to its original shape or position. The restoring force at the Lagrangean point is then distributed in the surrounding fluid (Eulerian grid point) as a body force, and the Navier-Stokes equations with body strength are resolved throughout the domain. The IBM was reviewed in [5], presenting there an extensive list of bibliographic references. The easy computational implementation of IBM has attracted many reseachers. Various modifications and refinements have been made. Among them, Lai and Peskin [6] presented a second-order accurate IBM and applied it to simulate the flow past a circular cylinder. The interaction between the fluid and immersed boundary was modeled by a suitable representative of the delta-function.

The work of Goldstein *et al.* [7] presents a method that uses control of the velocity on the solid boundary to enforce the boundary conditions, and demonstrates its suitability for a flow past a rigid cylinder. In the process of obtaining the forcing momentum term iteratively, two negative semi-empirically constants are required in the numerical scheme, creating severe stability problems in the computation. The forcing momentum and the parameters are used into nearby Eulerian grids [1],[2]–[7]. Instead of adopting user-specified parameters, the forcing term imposing a specific boundary condition on the body was numerically extracted, so this scheme can be classified as a discrete forcing approach.

The work of Yang [8] proposes the use of a methodology called Virtual Boundary Method (VBM): a bilinear interpolation procedure is combined to realize the data transmission between grid and boundary points. The selection of constant values in the forcing term is discussed based on the error of the velocity at the boundary. Then, the VBM method is used to simulate the flow around bluff bodies. The VBM feasibility is verified by the good agreement between the simulation's results and other reference's outcomes. Mohd-Yusof [9] introduced a momentum forcing term that does not affect the stability of the discrete-time equation. The need to use a small computational time step, which is regarded as an important advantage of this method over other previous methods, is therefore avoided. Ye *et al.* [10] proposed the so-called Cartesian grid method in non-staggered grids to simulate the unsteady and incompressible Navier-Stokes equations in the physical domain with complex immersed boundary. In the whole computational domain, a finite-volume method of second-order accuracy is applied together with the two-step fractional-step procedure. Near the immersed boundary, an interpolation procedure of second-order spatial accuracy is used.

The objectives of this study were to propose an immersed boundary method that accounts for both momentum and heat transfer during mixed convection, taking into consideration the onset of turbulence between a heated immersed body (referred to as an isothermal immersed body) and the surrounding fluid. Furthermore, the study aimed to analyze the effects resulting from the combination of these physical phenomena.. As far as we know, heat-transfer by mixed convection combined with the phenomena of turbulence around complex geometries is treated in a segregated way in many works, some of them considering only forced convection for low Reynolds numbers. Santos

et al. [11] present the IBM for low and high Reynolds numbers coupled with the Virtual Physical Model (VPM) proposed by Silva *et al.* [12] to calculate the Lagrangian force field, based only on the momentum equation. To simulate incompressible two-dimensional flows around heated square cylinders, a constant temperature was assumed on the surface of the cylinders. A good numerical agreement was achieved, with a margin of error of less than 3% compared to these previous works. The time evolution of the drag and lift coefficients, as well as, the Nusselt number, were obtained with this methodology, being the parameters obtained from the Eulerian fields. The geometry used in this work has singularities, which were taken into account in the construction of the algorithm/code. This fact holds significant importance as it enables its applicability to various geometries. Across all simulations, the results consistently indicate that the influence of the immersed heated body's surface on the flow intensifies with higher Reynolds numbers. A turbulence model was also used for transfer process between the largest and smallest turbulent scales.

For this work, we will consider Newtonian and incompressible fluids with constant properties. The buoyancy term based on the Boussinesq approximation is presented, considering the case of mixed convection. The momentum and heat transformations between the Lagrangian and Eulerian coordinates were realized by using a smooth Dirac delta-function, so that the nearby grid points are locally subject to momentum and heat transfer. The stability regimes were validated for two empirical constants. The governing equations were independently solved in each grid system coupled. The energy generation term is disregarded/ignored in this context, because neither the effects of internal heat (for example, absorption or emission radiation) nor the humidity (which could be responsible for the latent heat exchange) are considered. Coriolis force or rotation effects are also absent in this paper. The proposed methods were validated for natural and forced (mixed) convection, with the isothermal and constant heat flux boundary conditions. Finally, the heat-transfer and the onset of turbulence around complex geometry with the surrounding fluid was examined. The numerical results obtained are both accurate and stable, demonstrating a strong agreement with the existing findings in the literature.

2 Mathematical methodology

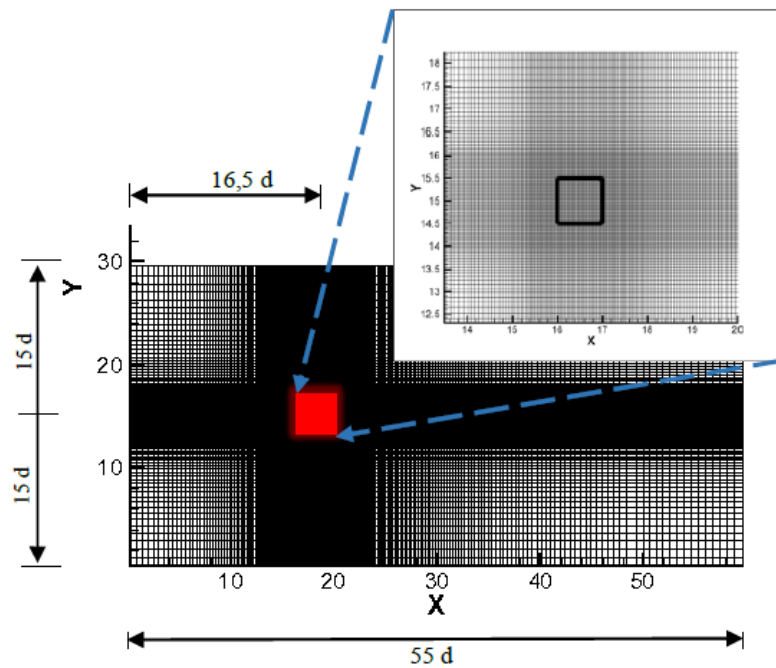### 2.1 Mathematical formulation for the fluid motion and temperature

Consider a viscous incompressible flow in a two-dimensional domain Ω containing an immersed boundary in the form of closed curve Γ, as shown in Fig. (1). Like in previous works, the forcing term is also introduced in the momentum equations and the heat source term is incorporated in the energy equation. As a result, the governing equations describing the forced/natural convection can be written in the primitive variables form as

$$\rho_0 \left(\frac{\partial \mathbf{u}}{\partial t} + (\mathbf{u} \bullet \nabla) \mathbf{u} \right) = -\nabla p + \mu \nabla^2 \mathbf{u} + \mathbf{f} \,, \tag{1}$$

$$\rho_0 \left(\frac{\partial \mathbf{u}}{\partial t} + (\mathbf{u} \bullet \nabla) \mathbf{u} \right) = -\nabla p + \mu \nabla^2 \mathbf{u} + \rho_0 \mathbf{g} \left(1 - \beta \left(T - T_\infty \right) \right) \mathbf{j} + \mathbf{f} \,, \qquad (2)$$

$$\rho_0 c_p \left(\frac{\partial T}{\partial t} + (\mathbf{u} \bullet \nabla) T \right) = k \nabla^2 T + q \,, \qquad (3)$$

$$\nabla \bullet \mathbf{u} = 0 \,, \qquad (4)$$

Fig. 1. A two-dimensional domain Ω containing an ishothermal bluff body (isothermal square cylinder) Γ with non-uniform grid.

where Eqs. (1), (3) and (4) are for forced convection, while Eqs. (2), (3) and (4) are for natural convection (in Eq. (2), the Boussinesq approximation is used). The symbols (i) $\mathbf{u}$, p, T and T_∞ denote velocity vector, pressure, temperature and reference temperature, respectively, (ii) ρ_0, μ, β, k and c_p are fluid density at temperature $T = T_\infty$, viscosity, thermal diffusivity, thermal expansion coeficient and specific heat at constant pressure, respectively, (iii) $\mathbf{g}$ is a downward gravitational acceleration, (iv) the term $\rho_0 \mathbf{g} \beta \left(T - T_\infty \right)$ accounts for the effects of the fluid temperature on the fluid flow, and (v) $\mathbf{j}$ is the unit vector in the positive y-axis direction, respectively.

The governing equations are non-dimensionalized by using characteristic scales such as the fluid density ρ_0 for the characteristic density, the far-field velocity U_∞ for the characteristic velocity, and the body diameter D for the characteristic length. The following characteristic scales are introduced: D/U_∞ for the time, $\rho_0 U_\infty^2$ for the pressure, and $\rho_0 U_\infty^2 / D$ for the Eulerian momentum force $\mathbf{f}$ or simply forcing term. The dimenionless incompressible Navier-Stokes equations and energy equation are

 R D. C. Santos; Q. G. Silva; S. R. L. Tananta

$$\frac{\partial \mathbf{u}}{\partial t} + (\mathbf{u} \cdot \nabla) \mathbf{u} = -\nabla p + \frac{1}{Re} \nabla^2 \mathbf{u} + \frac{Gr}{Re^2} \mathbf{g}T + \mathbf{f} \,, \tag{5}$$

$$\frac{\partial T}{\partial t} + \mathbf{u} \cdot \nabla T = \frac{1}{Re \cdot Pr} \nabla^2 T + q \,, \tag{6}$$

where Re is the Reynolds number, defined mathematically by $Re = \rho_0 U_\infty D / \mu$, and Gr is the Grashof number, defined here by $Gr = \mathbf{g}\beta (T - T_\infty) D^3 / \nu^2$. Pr denotes the Prandtl number, defined by $Pr = \nu/\alpha$, where α and ν are the thermal diffusivity and the kinematic viscosity, respectively. The non-dimensional continuity equation takes the same form as the dimensional continuity equation.

The forcing term $\mathbf{f}$ in the momentum Eqs. (1) and (2) is the force density at the fluid (Eulerian grid) point distributed from the force density at the boundary (Lagrangian) point, which can be expressed as

$$\mathbf{f}(\mathbf{x}, t) = \int_\Gamma \mathbf{F}(\mathbf{X}(s), t) \, \delta(\mathbf{x} - \mathbf{X}(s, t)) \, ds \,, \tag{7}$$

where $\mathbf{x}$ is the Eulerian coordinate. $\mathbf{X}$ and $\mathbf{F}$ stand for Lagrangian coordinate and the boundary force density respectively. $\delta(\mathbf{x} - \mathbf{X}(s, t))$ is the Dirac delta function representing the interaction between fluid and the immersed boundary. Similarly, the heat source/sink term q in the energy, Eq. (3), is the heat density transferred to the fluid from the heat flux at the immersed boundary, which can be written as

$$q(\mathbf{x}, t) = \int_\Gamma Q(\mathbf{X}(s), t) \, \delta(\mathbf{x} - \mathbf{X}(s, t)) \, ds \,. \tag{8}$$

Here, $Q(\mathbf{X}(s), t)$ is the virtual boundary heat flux.

The boundary condition-enforced immersed boundary method developed in this paper involves both velocity correction and temperature correction to satisfy the boundary conditions. In the following, the velocity correction procedure will be describe first, followed by the temperature correction procedure.

2.2 Velocity correction procedure

With the help of fractional step technique, the velocity field can be obtained in the following predictor-corrector steps:

(1) **Predictor step**:

We start with the usual Navier-Stokes equations without the forcing term,

$$\rho_0 \left(\frac{\partial \mathbf{u}}{\partial t} + (\mathbf{u} \bullet \nabla) \mathbf{u} \right) = -\nabla p + \mu \nabla^2 \mathbf{u} \,, \tag{9}$$

$$\rho_0 \left(\frac{\partial \mathbf{u}}{\partial t} + (\mathbf{u} \bullet \nabla) \mathbf{u} \right) = -\nabla p + \mu \nabla^2 \mathbf{u} + \rho_0 \mathbf{g} \left(1 - \beta \left(T - T_\infty \right) \right) \mathbf{j}, \tag{10}$$

By solving the above Eq. (9) or (10) together with Eq. (4), using the projection method developed by Chorin [13], we obtain the predicted velocity $\mathbf{u}^*$. The basic solution procedure is described as follows.

To advance the solution from time level n to $n+1$, the Crank-Nilson scheme is applied for temporal discretization, and the immediate velocity $\tilde{\mathbf{u}}$ can be given by

$$\rho_0 \frac{\tilde{\mathbf{u}} - \mathbf{u^n}}{\delta t} = -\frac{\rho_0}{2} \left[(\tilde{\mathbf{u}} \cdot \nabla) \tilde{\mathbf{u}} + (\mathbf{u^n} \cdot \nabla) \mathbf{u^n} \right] + \frac{\mu}{2} \left(\nabla^2 \tilde{\mathbf{u}} + \nabla^2 \mathbf{u^n} \right), \tag{11}$$

$$\rho_0 \frac{\tilde{\mathbf{u}} - \mathbf{u^n}}{\delta t} = -\frac{\rho_0}{2} \left[(\tilde{\mathbf{u}} \cdot \nabla) \tilde{\mathbf{u}} + (\mathbf{u^n} \cdot \nabla) \mathbf{u^n} \right] + \frac{\mu}{2} \left(\nabla^2 \tilde{\mathbf{u}} + \nabla^2 \mathbf{u^n} \right) + $$
$$\rho_0 \left(\frac{Gr}{Re^2} \right) \left(1 - \beta \left(T^\mathbf{n} - T_\infty \right) \right) \mathbf{j}. \tag{12}$$

Then, the immediate velocity $\tilde{\mathbf{u}}$ is corrected to the predicted velocity $\mathbf{u}^*$ by the following form

$$\rho_0 \frac{\mathbf{u}^* - \tilde{\mathbf{u}}}{\delta t} = -\nabla p^{n+1}. \tag{13}$$

The Richardson's number $(Ri = Gr/Re^2)$, present in Eq. (12), expresses the relationship between the buoyancy of a fluid in relation to its viscosity. In this work, the Richardson's number is based on the distance between two isothermal plates, $Gr = \mathbf{g}\beta \left(T - T_\infty \right) D^3/\nu^2$, which represent the walls of a computing domain, separated by a characteristic distance D. Before using Eq. (11), the pressure field should be obtained first by solving the following Poisson equation

$$\nabla^2 p^{n+1} = \rho_0 \frac{\nabla \cdot \tilde{\mathbf{u}}}{\delta t}. \tag{14}$$

In the implementation process, a staggered grid is used for the finite volume discretization of Eqs. (9) and (10), i.e. a scalar variable pressure-like is defined at the center of each cell, while velocity components are defined at the cell faces. For the spatial derivatives, the well-know central difference scheme is employed.

(2) **Corrector step:**

The corrected velocity field can be obtained by solving the following equation with the force term $\mathbf{f}$,

$$\rho \frac{\partial \mathbf{u}}{\partial t} = \mathbf{f}. \tag{15}$$

In the conventional IBM, the force density $\mathbf{f}$ is determined in advance and then the corrected velocity $\mathbf{u}$ can be obtained from Eq. (15). However, there is no guarantee that the velocity at the Lagrangian point interpolated from this corrected velocity $\mathbf{u}$ always satisfies the non-slip boundary condition. This drawback can be overcome by the present method. The basic idea is that the force density $\mathbf{f}$ is considered as unknown, which is evaluated implicitly in such a way that the velocity $\mathbf{u}\left(\mathbf{X}\left(s\right),t\right)$ at the boundary (Lagrangian) point interpolated from the corrected velocity $\mathbf{u}$ at the Eulerian grids equals the given boundary velocity $\mathbf{U}_B$. By applying forward Euler method to approximated the temporal derivative in Eq. (15), it is clear that adding a forcing term $\mathbf{f}$ is equivalent to making a correction $\delta\mathbf{u}$ in the velocity field. By defining

$$\mathbf{u} = \mathbf{u}^* + \delta\mathbf{u}. \tag{16}$$

The Eq. (15) gives

$$\rho\frac{\delta\mathbf{u}}{\delta t} = \mathbf{f}, \tag{17}$$

where δt is the time step size, $\mathbf{u}$ is the corrected velocity, $\mathbf{u}^*$ is the intermediate velocity, $\delta\mathbf{u}$ is the velocity correction. Suppose that the immersed boundary is represented by a set of Lagrangian points $\mathbf{X}_B^i$ $(i = 1, 2, \cdots, M)$, and the fluid field is covered by a fixed uniform Cartesian mesh $\mathbf{x}_j$ $(j = 1, 2, \cdots, N)$ with mesh spacing $\Delta x = \Delta y = h$. Furthermore, let $\delta\left(\mathbf{x} - \mathbf{X}\left(s,t\right)\right)$ be smoothly approximated by a continous kernel distribution

$$D_{ij} = D\left(\mathbf{x}_j - \mathbf{X}_B^i\right) = \frac{1}{h^2}\delta\left(\frac{x_j - X_B^i}{h}\right)\delta\left(\frac{y_j - Y_B^i}{h}\right). \tag{18}$$

Here, h is the mesh size of Eulerian mesh, and $\delta\left(r\right)$ is proposed by Lai and Peskin [13]

$$\delta\left(r\right) = \begin{cases} \frac{1}{8}\left(3 - 2\left|r\right| + \sqrt{1 + 4\left|r\right| - 4r^2}\right) & , & \left|r\right| \leqslant 1 \\ \frac{1}{8}\left(5 - 2\left|r\right| + \sqrt{-7 + 12\left|r\right| - 4r^2}\right) & , & 1 < \left|r\right| \leqslant 2 \\ 0 & , & \left|r\right| > 2. \end{cases} \tag{19}$$

Note from Eq. (7) that the force density $\mathbf{f}$ at the Eulerian point is distributed from the boundary force $\mathbf{F}$ through the Dirac delta function $\left(\delta\left(\mathbf{x} - \mathbf{X}\left(s,t\right)\right)\right)$ interpolation. Eq. (7) can be written in the discrete form as

$$\mathbf{f}\left(\mathbf{x}_j, t\right) = \sum_i \mathbf{F}\left(\mathbf{X}_B^i, t\right) D\left(\mathbf{x}_j - \mathbf{X}_B^i\right)\Delta s_i, \qquad (j = 1, 2, \cdots, N; i = 1, 2, \cdots, M). \tag{20}$$

Substituting Eq. (20) into Eq. (17), we have

$$\delta \mathbf{u}\left(\mathbf{x}_j, t\right) = \sum_i \frac{\mathbf{F}\left(\mathbf{X}_B^i, t\right) \delta t}{\rho} D\left(\mathbf{x}_j - \mathbf{X}_B^i\right) \Delta s_i, \qquad (i = 1, 2, \cdots, M), \qquad (21)$$

where $\delta \mathbf{u}\left(\mathbf{x}_j, t\right)$ is the velocity correction at the jth Eulerian point, Δs_i is the ith boundary segmente length. It is noted that the known quantities in Eq. (21) are the boundary forces $\mathbf{F}_B^i$ (abbreviation for $\mathbf{F}\left(\mathbf{X}_B^i, t\right)$). To satisfy the non-slip boundary condition, the velocity at the boundary point interpolated from the corrected fluid velocity field via the smooth delta function D_{ij} must be equal to the boundary velocity $\mathbf{U}\left(\mathbf{X}_B^i, t\right)$ at the same position

$$\mathbf{U}\left(\mathbf{X}_B^i, t\right) = \sum_j \mathbf{u}\left(\mathbf{x}_j, t\right) D\left(\mathbf{x}_j - \mathbf{X}_B^i\right) h^2, \qquad (j = 1, 2, \cdots, N). \qquad (22)$$

Here, $\mathbf{u}\left(\mathbf{x}_j, t\right)$ is the corrected velocity at the jth Eulerian grid point, expressed as the sum of predicted velocity $\mathbf{u}^*\left(\mathbf{x}_j, t\right)$ and velocity correction $\delta \mathbf{u}\left(\mathbf{x}_j, t\right)$

$$\mathbf{u}\left(\mathbf{x}_j, t\right) = \mathbf{u}^*\left(\mathbf{x}_j, t\right) + \delta \mathbf{u}\left(\mathbf{x}_j, t\right). \qquad (23)$$

Substituting Eqs. (23) and (21) into Eq. (22), gives

$$\mathbf{U}\left(\mathbf{X}_B^i, t\right) = \sum_j \mathbf{u}^*\left(\mathbf{x}_j, t\right) D\left(\mathbf{x}_j - \mathbf{X}_B^i\right) h^2 +$$
$$\sum_j \sum_k \frac{\mathbf{F}\left(\mathbf{X}_B^i, t\right) \delta t}{\rho} D\left(\mathbf{x}_j - \mathbf{X}_B^k\right) \Delta s_k D\left(\mathbf{x}_j - \mathbf{X}_B^i\right) h^2, \quad (24)$$

for $i = 1, 2, \cdots, M; \; j = 1, \cdots, N; \; k = 1, \cdots, M$.

The system of equations for the boundary force can be written in the following matrix form

$$\mathbf{A}\,\mathbf{X} = \mathbf{B}, \qquad (25)$$

where

$$\mathbf{A} = \frac{\delta t}{\rho} h^2 \begin{pmatrix} D_{11}\Delta s_1 & D_{12}\Delta s_1 & \cdots & D_{1N}\Delta s_1 \\ D_{21}\Delta s_2 & D_{22}\Delta s_2 & \cdots & D_{2N}\Delta s_2 \\ \vdots & \vdots & \ddots & \vdots \\ D_{M1}\Delta s_M & D_{M2}\Delta s_M & \cdots & D_{MN}\Delta s_M \end{pmatrix} \begin{pmatrix} D_{11} & D_{12} & \cdots & D_{1M} \\ D_{21} & D_{22} & \cdots & D_{2M} \\ \vdots & \vdots & \ddots & \vdots \\ D_{N1} & D_{N2} & \cdots & D_{NM} \end{pmatrix}$$
$$(26)$$

$$\mathbf{B} = \begin{pmatrix} \mathbf{U}_B^1 \\ \mathbf{U}_B^2 \\ \vdots \\ \mathbf{U}_B^M \end{pmatrix} - h^2 \begin{pmatrix} D_{11} & D_{12} & \cdots & D_{1M} \\ D_{21} & D_{22} & \cdots & D_{2M} \\ \vdots & \vdots & \ddots & \vdots \\ D_{N1} & D_{N2} & \cdots & D_{NM} \end{pmatrix} \begin{pmatrix} \mathbf{u}_1^* \\ \mathbf{u}_2^* \\ \vdots \\ \mathbf{u}_N^* \end{pmatrix} \qquad (27)$$

$$\mathbf{X} = \begin{pmatrix} \mathbf{F}_B^1 \\ \mathbf{F}_B^2 \\ \vdots \\ \mathbf{F}_B^M \end{pmatrix} \qquad (28)$$

and $\mathbf{U}_B^i$ $(i = 1, \cdots, M)$, $\mathbf{u}_j^*$ $(j = 1, \cdots, N)$ are the abbreviations for $\mathbf{U}\left(\mathbf{X}_B^i, t\right)$ and $\mathbf{u}^*\left(\mathbf{x}_j, t\right)$, respectively. In this way, the boundary force $\mathbf{F}_B^i$ $(i = 1, \cdots, M)$ is evaluated directly and implicity so that the satisfying of no-slip condiction is accurately achieved. It can be observed that the entries of matrix $\mathbf{A}$ depend only on the coordinate information of the Lagrangian boundary points and their adjacent Eulerian points. By solving the equation system (26), using a direct method or iteractive method, the unknow boundary force $\mathbf{F}_B^i$ $(i = 1, \cdots, M)$ at all Lagrangian boundary points are obtained simultaneously, which are then substituted into Eqs. (21) and (23) to calculate the velocity correction $\delta\mathbf{u}_j$ and the corrected velocity $\mathbf{u}_j$ $(j = 1, \cdots, N)$.

A remarkable advantage of the present method is that the force on the Lagrangian points can be directly derived, since it is a part of the solution. We know that $\mathbf{F}_B^i$ $(i = 1, \cdots, M)$ is the boundary force density acting on the fluid, and due to the fact that action and reaction are equal and opposite, it is obvious that the force exerceted by fluid on the boundary should be $-\mathbf{F}_B^i$ $(i = 1, \cdots, M)$ at each Lagrangian point.

2.3 Temperature correction procedure

Similarly, using the fractional step approach, the solution of Eq. (3) can be also obtained by predictor-corrector steps. The predictor step solves the following energy equation without the heat source term q,

$$\rho_0 c_p \left(\frac{\partial T}{\partial t} + (\mathbf{u} \bullet \nabla) T\right) = k\nabla^2 T. \qquad (29)$$

The resultant solution from Eq. (29) is noted as predicted temperature $T^*(x, t)$, which can be obtained by solving the following equation obtained by the Crank-Nicolson scheme

$$\rho_0 c_p \frac{T^* - T^n}{\delta t} = -\frac{\rho_0 c_p}{2}\left[\left(\mathbf{u}^{n+1} \cdot \nabla\right) T^* + \left(\mathbf{u}^{n+1} \cdot \nabla\right) T^n\right] + \frac{k}{2}\left(\nabla^2 T^* + \nabla^2 T^n\right). \qquad (30)$$

Similar to the velocity correction procedure, the corrected temperature $T(\mathbf{x}, t)$ is obtained by solving the following equation,

$$\rho_0 c_p \frac{\partial T}{\partial t} = q \,. \tag{31}$$

It can be clearly observed from Eq. (31) that adding a heat source/sink is equivalente to making a temperature correction. Applying Euler explicit scheme to Eq. (31) gives

$$\rho_0 c_p \frac{\delta T}{\delta t} = q \,, \tag{32}$$

with

$$\delta T\left(\mathbf{x}, t\right) = T\left(\mathbf{x}, t\right) - T^*\left(\mathbf{x}, t\right) \,, \tag{33}$$

where $\delta T\left(\mathbf{x}, t\right)$ is the temperature correction and $T\left(\mathbf{x}, t\right)$ is the corrected temperature. Note from Eq. (8) that the heat source/sink, q, at the Eulerian grid point is distributed from the boundary heat flux, Q, through Dirac delta function interpolation, which can be expressed in the discret form as

$$q\left(\mathbf{x}_j, t\right) = \sum_i Q\left(\mathbf{X}_B^i, t\right) D\left(\mathbf{x}_j - \mathbf{X}_B^i\right) \Delta s_i \,, \qquad (i = 1, \cdots, M; \, j = 1, \cdots, N) \,. \tag{34}$$

Substituting Eq. (33) into Eq. (32) leads to

$$\delta T\left(\mathbf{x}_j, t\right) = \sum_i \frac{Q\left(\mathbf{X}_B^i, t\right) \delta t}{\rho c_p} D\left(\mathbf{x}_j - \mathbf{X}_B^i\right) \Delta s_i \,, \qquad (i = 1, \cdots, M; \, j = 1, \cdots, N) \,. \tag{35}$$

It is noted that the unknows in Eq. (35) are the boundary heat fluxes $Q\left(\mathbf{X}_B^i, t\right)$. To satisfy the physical boundary condiction, we have to make sure that the temperature at the boundary point interpolated from the corrected temperature field by the delta function D_{ij} is equal to the specified temperature $T_B\left(\mathbf{X}_B^i, t\right)$, that is,

$$T_B\left(\mathbf{X}_B^i, t\right) = \sum_j T\left(\mathbf{x}_j, t\right) D\left(\mathbf{x}_j - \mathbf{X}_B^i\right) h^2 \quad (i = 1, \cdots, M; \, j = 1, \cdots, N) \,. \tag{36}$$

Substituting Eqs. (33) and (35) into Eq. (36) gives

$$T_B\left(\mathbf{X}_B^i, t\right) = \sum_j T^*\left(\mathbf{x}_j, t\right) D\left(\mathbf{x}_j - \mathbf{X}_B^i\right) h^2 +$$

$$\sum_j \sum_k \frac{Q\left(\mathbf{X}_B^k, t\right) \delta t}{\rho c_p} D\left(\mathbf{x}_j - \mathbf{X}_B^k\right) \Delta s_k D\left(\mathbf{x}_j - \mathbf{X}_B^i\right) h^2 \,, \tag{37}$$

with $i = 1, \cdots, M; \, j = 1, \cdots, N$. The Eq. (37) can be put in the following matrix form

$$\mathbf{C}\,\mathbf{Y} = \mathbf{D}\,, \tag{38}$$

where

$$\mathbf{C} = \frac{\delta t}{\rho c_p} h^2 \begin{pmatrix} D_{11}\Delta s_1 & D_{12}\Delta s_1 & \cdots & D_{1N}\Delta s_1 \\ D_{21}\Delta s_2 & D_{22}\Delta s_2 & \cdots & D_{2N}\Delta s_2 \\ \vdots & \vdots & \ddots & \vdots \\ D_{M1}\Delta s_M & D_{M2}\Delta s_M & \cdots & D_{MN}\Delta s_M \end{pmatrix} \begin{pmatrix} D_{11} & D_{12} & \cdots & D_{1M} \\ D_{21} & D_{22} & \cdots & D_{2M} \\ \vdots & \vdots & \ddots & \vdots \\ D_{N1} & D_{N2} & \cdots & D_{NM} \end{pmatrix} \tag{39}$$

$$\mathbf{D} = \begin{pmatrix} T_B^1 \\ T_B^2 \\ \vdots \\ T_B^M \end{pmatrix} - h^2 \begin{pmatrix} D_{11}\Delta s_1 & D_{12}\Delta s_1 & \cdots & D_{1N}\Delta s_1 \\ D_{21}\Delta s_2 & D_{22}\Delta s_2 & \cdots & D_{2N}\Delta s_2 \\ \vdots & \vdots & \ddots & \vdots \\ D_{M1}\Delta s_M & D_{M2}\Delta s_M & \cdots & D_{MN}\Delta s_M \end{pmatrix} \begin{pmatrix} T_B^* \\ T_2^* \\ \vdots \\ T_N^* \end{pmatrix} \tag{40}$$

$$\mathbf{Y} = \begin{pmatrix} Q_B^1 \\ Q_B^2 \\ \vdots \\ Q_B^M \end{pmatrix} \tag{41}$$

with $T_B^i\ (i = 1, \cdots, M)$, $T_j^*\ (j = 1, \cdots, N)$ and $Q_B^i\ (i = 1, \cdots, M)$, representing $T\left(\mathbf{X}_B^i, t\right)$, $T^*\left(\mathbf{x}_j, t\right)$ and $Q\left(\mathbf{X}_B^i, t\right)$, respectively.

As shown above, the essence of temperature correction procedure is that the heat source/sink is determined implicitly in such a way that the temperature $T\left(\mathbf{X}\left(s\right), t\right)$ at the boundary point interpolated from the corrected temperature field $T\left(\mathbf{x}, t\right)$ equals to the specified boundary temperature T_B. In other words, the physical boundary condition is enforced. The system of linear equations (38) can be solved by a direct method or an interactive method. After Q_B^i at all Lagrangian points are obtained, they are then substituted into Eq. (35) to obtain the temperature correction δT_j, which are further substituted into Eq. (33) to get finally the corrected temperature $T_j\ (j = 1, \cdots, N)$.

3 Evaluating the average number of Nusselt

Nusselt number is a key parameter in the heat-transfer problem. The local Nusselt number Nu is defined as

$$Nu\left(\mathbf{X}\left(s\right),t\right) = \frac{h\left(\mathbf{X}\left(s\right),t\right)L_c}{k}, \tag{42}$$

where L_c is a typical characteristic length. According to Newton's cooling law and Fourier's law, the heat conducted away from the wall by the fluid is equal to the heat convection from the wall, that is

$$-k\frac{\partial T}{\partial n}\left(\mathbf{X}\left(s\right),t\right) = h\left(\mathbf{X}\left(s\right),t\right)\left(T_w - T_\infty\right). \tag{43}$$

Substituting Eq. (43) into Eq. (42) one obtains

$$Nu\left(\mathbf{X}\left(s\right),t\right) = \frac{1}{T_w - T_\infty}\frac{-k\frac{\partial T}{\partial n}\left(\mathbf{X}\left(s\right),t\right)L_c}{k} = -\frac{L_c}{T_w - T_\infty}\frac{\partial T}{\partial n}\left(\mathbf{X}\left(s\right),t\right). \tag{44}$$

The average Nusselt number $\overline{Nu}$ is an important parameter to examine the rate of heat-transfer from the heated surface and is defined by

$$\overline{Nu} = \frac{1}{L}\int_\Gamma Nu \cdot ds = \frac{1}{L}\int_\Gamma -\frac{L_c}{T_w - T_\infty}\frac{\partial T}{\partial n}\left(\mathbf{X}\left(s\right),t\right)ds, \tag{45}$$

where $L = \int_\Gamma ds$ is the total length of the immersed boundary. As shown in Eq. (44) and (45), the evaluation of the local and average Nusselt numbers involves the calculation of the temperature gradient at the boundary points.

3.1 Estimation of the average Nusselt at Eulerian points

As shown in Eq. (8), the heat source at one Eulerian points is from the heat flux at a few Lagrangian points. If we consider all the Eulerian points which receive the heat from the immersed boundary, then from energy conservation law, we have

$$\int_\Omega q\left(\mathbf{x},t\right)d\mathbf{x} = \int_\Gamma Q\left(\mathbf{X}\left(s\right),t\right)ds, \tag{46}$$

in which the l.h.s. (left hand side) is the volume integral in the whole fluid domain, and the r.h.s. (right hand side) is the surface integral along the cylinder wall. According to Fourier's law, $Q\left(\mathbf{X}\left(s\right),t\right)$ can be written as

$$Q\left(\mathbf{X}\left(s\right),t\right) = -k\frac{\partial T}{\partial n}\left(\mathbf{X}\left(s\right),t\right). \tag{47}$$

Substituting Eqs. (32) and (47) into Eq. (46) gives

$$\int_{\Omega} \rho c_p \frac{\delta T}{\delta t} d\mathbf{x} = \int_{\Gamma} -k \frac{\partial T}{\partial n} \left(\mathbf{X} \left(s \right), t \right) ds .$$ (48)

The r.h.s. of Eq. (48) can be also be written in terms of local Nusselt numbers $Nu\left(\mathbf{X}\left(s\right),t\right)$ as

$$\int_{\Gamma} -k \frac{\partial T}{\partial n} \left(\mathbf{X} \left(s \right), t \right) ds = \int_{\Gamma} \frac{k \cdot Nu\left(\mathbf{X}\left(s\right)t\right)\left(T_w - T_\infty\right)}{L_c} ds = \frac{\overline{Nu}\left(T_w - T_\infty\right)kL}{L_c}$$ (49)

Eq. (48) can then be simplified to

$$\frac{\overline{Nu}\left(T_w - T_\infty\right)}{L_c} kL = \int_{\Omega} \rho c_p \frac{\delta T}{\delta t} d\mathbf{x} .$$ (50)

Thanks to the approximation of the volume integral offered by the mean theorem, the equality (50) can be finally written as

$$\overline{Nu} = \frac{\sum_j \rho c_p \frac{\delta T_j}{\delta t} \Delta x_j \Delta y_j}{kL\left(T_w - T_\infty\right)} L_c , \qquad (j = 1, \cdots, N) .$$ (51)

In Figs. (2) and (3), we present the behaviour of the flow around the neighborhood of the ishotermal square cylinder (bluff body) at different values of Re ($Re = 1, 2$ and $Re = 10$) and Ri ($Ri = 0$ and $Ri = 0, 5$).

(a)   (b)
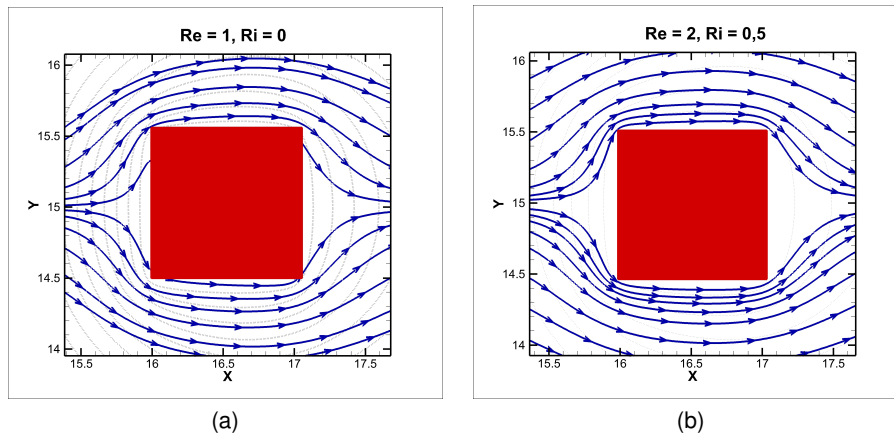
Fig. 2. Streamlines for flow around ishotermal square cylinder at $Re = 1$ and $Re = 2$ for different Richardson numbers (Ri).
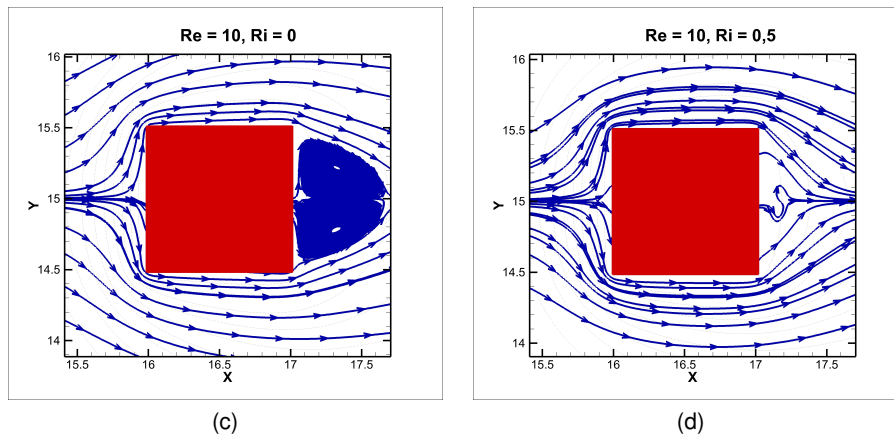
Fig. 3. Streamlines for flow around ishotermal square cylinder at $Re = 10$ for different Richardson numbers (Ri).

The fluid begins the process of separation of bluff body when $Re \geq 2$, for different Ri values. A detachment process from the circulation bubble is also observed in Fig. (2-(**c**)) for $Re = 10$ with $Ri = 0$.

Other works using different numerical methodologies have presented a similar scenario; for example, see Chatterjee [14], where it is conducted a study for a pair of square cylinders in a *tandem* vertical channel configuration, with low Reynolds numbers. Here, the author concluded that the beginning of separation of the flow occurs for $Re = 1 - 2$, $Re = 2 - 3$ and $Re = 3 - 4$, considering the same values for the Richardson number presented in our work. Therefore, in this work, it was observed that, as the Reynolds number is (gradually) increased, the separation of the flow occurs at the trailing edge of the immersed ishotermal body and the two (symmetrical) vortices of the recirculation bubble begin to be formed downstream of the obstacle, even under the permanent outflow regime. This can be attributed to the increase in buoyancy, which leads to a higher velocity gradient on the surface of the cylinder. Consequently, the pressure on the immersed body's surface decreases. Other significant studies, including Singh [15] and Moulay [16], in addition to presenting similar scenarios, there is a critical value to be studied for the adimensionless number Ri, i.e. the authors take into account the onset of the vortex detachment and analyze the influence of this parameter with the increase of Re.

Table 1. Comparison of drag coefficiet (C_d) and average Nusselt (Nu) numbers for isothermal boundary condition, for different Reynolds (Re) numbers.

	Re	Cd	Nu
Present	1	4,8500	0,6917
Anjaiah *et. al.* [17]	1	4,8600	0,6916
Dhiman *et. al.* [18]	1	4,8714	0,6916
Sharma *et. al.* [19]	1	4,8714	0,6928
Present	10	0,9300	1,5532
Anjaiah *et. al.* [17]	10	0,9437	1,5624
Continued on next page			

Table 1 – continued from previous page

Dhiman *et. al.* [18]	10	0,9437	1,5624
Sharma *et. al.* [19]	10	0,9343	1,5573
Present	40	0,2497	2,6802
Anjaiah *et. al.* [17]	40	0,2538	2,6969
Dhiman *et. al.* [18]	40	0,2538	2,6969
Sharma *et. al.* [19]	40	0,2493	2,6012

Note that the r.h.s. of Eq. (51) are dimensionless. The actual form of Eq. (51) for dimensionless variables depend on the reference characteristics taken for the problem considered. In the numerical studies reported below, the specific forms of Eq. (51) will be given.

The heat flux at Lagrangian points obtained from equation system (38) can be directly used to compute the average Nusselt number, that is,

$$\overline{Nu} = \frac{1}{L} \int_\Gamma \frac{L_c}{k \left(T_w - T_\infty\right)} \mathbf{Q}\left(\mathbf{X}\left(s\right), t\right) ds \, . \tag{52}$$

The the discretized form of Eq. (52) is

$$\overline{Nu} = \frac{\sum_i Q_B^i \Delta s_i}{kL \left(T_w - T_\infty\right)} L_c \, , \qquad \left(i = 1, \cdots, M\right) \, . \tag{53}$$

Note that Eq. (53) is also based on dimensionless, variables. Its specific form for dimensionless variables will be provided in Section 5.

4 Onset of turbulence

In addition to laminar regime flow, we have also simulated (onset of turbulence) flows for Reynolds numbers going up to 5×10^2. Thus, it is necessary to use turbulence models to close the Navier-Stokes equations. A model has been implemented, namely the Spalart-Allmaras model, with URANS model (Unsteady Reynolds Averaged Navier-Stokes).

The URANS model is used to refer to RANS (Reynolds Averaged Navier-Stokes), where in this model, the dependent variables of the Navier-Stokes equation are decomposed into filtered components and floating components, and then all terms are filtered.

4.1 Spalart-Allmaras model

The Spalart-Allmaras model is a one-equation model that solves the transport equation for the kinematic eddy turbulent viscosity [29], without involving turbulent energy, dissipation or vorticity calculations, available in other models. Thus, the Spalart-Allmaras model concentrates into a single parameter the behavior of turbulence, being classified as a closed model.

The equation for the turbulent viscosity is constructed using mainly flow empirical considerations, dimensional analysis and Galileo's principle of relativity. The model uses a working variable, $\widetilde{\nu}$, given by the following transport equation

$$\frac{\partial \widetilde{\nu}}{\partial t} + \frac{\partial}{\partial x_j}\left(u_j\widetilde{\nu}\right) = c_{b_1}\left(1 - f_{t_2}\right)\widetilde{S}\ \widetilde{\nu} + \frac{1}{\sigma}\left[\frac{\partial}{\partial x_j}\left(\left(\nu + \widetilde{\nu}\right)\frac{\partial \widetilde{\nu}}{\partial x_j}\right) + c_{b_2}\frac{\partial \widetilde{\nu}}{\partial x_j}\frac{\partial \widetilde{\nu}}{\partial x_j}\right]$$
$$- \left[c_w f_w - \frac{c_{b_1}}{k^2}f_{t_2}\right]\left[\frac{\widetilde{\nu}}{d_w}\right]^2 + f_{t_1}\Delta U^2\,,$$

(54)

where the terms on the right side are, respectively: the production of turbulent viscosity, the molecular and turbulent diffusion of $\widetilde{\nu}$, the dissipation of $\widetilde{\nu}$, the destruction of $\widetilde{\nu}$, which reduces the turbulent viscosity near the wall, and, finally, the terms that model the transition effects, indicated by sub-index t. The turbulence viscosity, ν_t, is calculated from the auxiliary variable of the Spalart-Allmaras model and damped by the function f_{v1} along the wall, and is given by:

$$\nu_t = \widetilde{\nu}f_{v_1}\,,$$

(55)

where

$$f_{v_1} = \frac{\chi^3}{\chi^3 + C_{v_1}^3}\,,$$

(56)

with

$$\chi = \frac{\widetilde{\nu}}{\nu}\,.$$

(57)

5 Results

5.1 Mixed convection around a isothermal cylinder

Forced convection over an isothermal cylinder has been extensively studied and used as a benchmark to examine the capability of numerical methods. The experimental [27] and numerical [17]-[26] results are available for square cylinder. The fluid and heat flow are characterized by Reynolds number $Re = \rho U_\infty D/\mu$ and Prandtl number $Pr = \mu c_p/k$, where ρ is the fluid density, U_∞ is the free stream velocity, D is the cylinder diameter, μ is the dynamic viscosity, c_p is heat at constant pressure and k the thermal diffusivity. In this work, numerical simulations are conducted for different low Reynolds numbers $Re = 1 - 500$, while keeping the Prandtl number fixed at $Pr = 0.7$. Both heat and fluid flow characteristics like the drag coefficient C_d, recirculation behind the cylinder, streamline and isotherm patterns, average Nusselt number on the cylinder surface are presented and compared with previous results in the literature.

A schematic view of two-dimensional heat and fluid flow across a heated square cylinder is shown in Fig. (1). In the simulation, governing equations in dimensionless form are used. The free-stream velocity U_∞ and the cylinder diameter D are chosen as the reference velocity and reference length, respectively. The temperature is normalized by

$$T^* = \frac{T - T_\infty}{T_c - T_\infty}\,,$$

(58)

where T_c is the temperature on the cylinder surface and T_∞ is the free-stream temperature. The specific dimensionless forms to compute the average Nusselt number by the methods 1 and 2 abovementioned, are

$$\overline{Nu} = \frac{Re \cdot Pr}{\pi} \sum_j \frac{\delta T_j}{\delta t} \Delta x_j \Delta y_i \,, \qquad (j = 1, \cdots, N) \,, \tag{59}$$

and

$$\overline{Nu} = \frac{\sum_i Q_B^i \Delta s_i}{\pi} \,, \qquad (i = 1, \cdots, M) \,, \tag{60}$$

respectively. Note that in Eq. (59), the dimensionless form of Q_B^i is actually $-\dfrac{\partial T}{\partial n}(\mathbf{X}_B^i, t)$, which can be directly obtained from the solution of equation system (38). The drag coefficient is defined as

$$C_d = \frac{F_d}{^{1}\!/_{2} \ \rho U_\infty^2 D} \,, \tag{61}$$

where F_d is the drag force that, in the present work, it is computed from the solution of equation system (25), which makes the drag force calculation very easy. In the order to validade our code, simulations with a single heated square cylinder were compared with the results found in the literature. To mimic free boundary conditions, it was considered $L_x = 55d$ and width $L_y = 30d$. The heated isothermal square cylinder was placed at $x = 16.5d$ and $y = 15d$, to minimize boundary influence. The grid resolution for these simulations was 318×164, 840×600 and 1120×800 points, a non-uniform grid was used to better capture the effects with a total of 202 Lagrangian grid points inside the immersed body. The grid is uniform in the region of the cylinder, maintaining a minimum number of 30 grid inside. The time step used in the calculation process is in the range $1.0 \times 10^{-6}s$ to $1.0 \times 10^{-4}s$, which is dynamically calculated by the Courant-Friedrichs-Lewy (CFL) condition:

$$CFL = \frac{\max \left(|u| + c\right)_{[x_j - 0.5, \, x_j + 0.5]} \times \Delta t}{\Delta x_j} \,. \tag{62}$$

To avoid numerical problems, the maximum ratio of 3% grid expansion was employed in this region in both directions. In the present work, the ratio between Lagrangian and Eulerian grid size was maintained at 0.98. The boundary condition were prescribed as follow: 1) uniform and nonuniform flow with velocity U_∞, pressure $p = 0$, and temperature $T_{input} = 0$ at the entrance of the domain (left side); 2) flow fully developed in the output ($\partial u / \partial x = 0$, $\partial T / \partial x = 0$); 3) condition of symmetries at the upper and lower boundaries ($\partial u / \partial y = v = 0$), ($\partial T / \partial y = 0$). Concerning the initial condition, we have considered $u = v = 0$, at $t = 0$ (time), for the entire computational domain. The square cylinder is maintained at a constant dimensionless temperature equal to 1, i. e.,

$T_c = 1$, while the fluid has an initial temperature equal to zero ($T_f = 0$). Although the boundary condition at the output is not a reflexive condition, the simulation results successfully corroborate the formation of large (vortex) structure outside the domain without any reflection. The current pressure boundary conditions at the inlet and outlet are imposed to ensure consistency with the equations for velocities, which is achieved through the arrangement of the staggered grid.

5.2 Mixed convection around isothermal cylinders in *tandem*

In this section, the flow around a pair of heated circular cylinders with different configurations is studied, where the heat transfer process around obstacles has its importance and relevance in engineering problems. Here, two cylinder configurations will be considered, where in both cases the two cylinders have equal diameters and the same center-to-center distance (L_{cc}). In the first case, the angle formed by the segment joining the centers of the two cylinders and the axis of the abscissa is zero.

5.2.1 Description of the problem and boundary conditions

In the Fig. (4) the two cylinders are identical and fixed with the same diameter, maintained in tandem configuration, the cylinder B, downstream of the cylinder A.
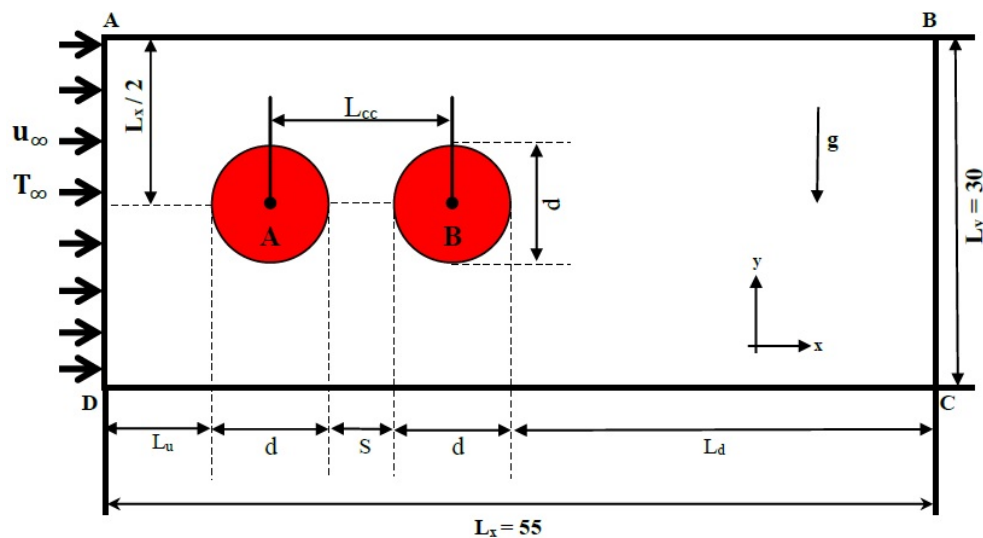

Fig. 4. Ilustration of the computational domain with two cylinders in tandem configuration.

In this case, the cylinders is confined to a channel with free flow, with uniform velocity (U_∞) and constant temperature ($T_c\,(> T_\infty)$). The horizontal and vertical spacing between the cylinders are fixed in $L_u = 16.5d$ and $L_d = 19.5d$, repectively. These values are chosen to reduce the effect of boundary condictions on the inlet and outlet relative to the flow pattern at the cylinder boundary. Moreover, these choices are also consistent with other contemporary works available in the literature, such as, for example, Mahir and Altaç [30], Sohankar and Etminan [26], Santos [32], Laidoudi and Bouzit [33] and Santos *et. al.* [11]. The drag (C_d) and lift (C_l) coefficients for the calculation of the each cylinder are performed as follows:

$$C_d = C_{dp} + C_{dv} = \frac{2F_d}{\rho U_\infty^2 d}, \tag{63}$$

$$C_l = C_{lp} + C_{lv} = \frac{2F_l}{\rho U_\infty^2 D}, \tag{64}$$

where C_{lp} and C_{lv} represent the lift coeficients due to pressure and viscous forces, respectively.

In a similar way, C_{dp} and C_{dv} represent the drag coeficients due to the pressure and viscous forces. F_d and F_l are forces of drag and lift, respectively, acting on the surface of the cylinder. Thus, the drag and lift coefficients can be obtained from the expressions:

$$\begin{cases} C_{dp} = 2\int_0^1 (p_f - p_r)\,dy\,, \\ \\ C_{dv} = \dfrac{2}{Re}\int_0^1 \left[\left\{ \left(\dfrac{\partial u}{\partial y}\right)_s + \left(\dfrac{\partial u}{\partial y}\right)_i \right\} dx + \left\{ \left(\dfrac{\partial u}{\partial x}\right)_f + \left(\dfrac{\partial u}{\partial x}\right)_r \right\} dy \right], \end{cases} \tag{65}$$

$$\begin{cases} C_{lp} = 2\int_0^1 (p_i - p_s)\,dy\,, \\ \\ C_{lv} = \dfrac{2}{Re}\int_0^1 \left[\left\{ \left(\dfrac{\partial v}{\partial x}\right)_f + \left(\dfrac{\partial v}{\partial x}\right)_b \right\} dx + \left\{ \left(\dfrac{\partial v}{\partial y}\right)_t + \left(\dfrac{\partial v}{\partial y}\right)_i \right\} dy \right]. \end{cases} \tag{66}$$

The subscripts f, b, i and s refer to "front", "back", "bottom" and "top" surfaces of the cylinders, respectively.

The main results for the simulations can be summarized as follows:

- A wake is formed upstream of the second cylinder, and it is necessary to investigate whether it can be reduced or eliminated by increasing the distance between the cylinders;

- The isothermal lines reflect the same behavior of the pattern of the streamlines (current lines);

- The average Nusselt number increase for $Re = 500$ for different values of Ri, even keeping the distance between the cylinders;

- The thermal buoyancy is suppressed in the recirculation zones of the tandem cylinders, even with a mounting angle;

- The thermal buoyancy tends to increase the coefficient of drag and the average Nusselt number of the cylinder more than the second;

5.2.2 Variations of the Nusselt number

One of the main objectives of heat-transfer calculations involving cylinders is to determine the local and overall heat-transfer around isothermal cylinders. The effect of the flow, especially regarding the heat-transfer, can be better observed by analyzing the local heat-transfer coeffient, also known as the Nusselt local number.

In the Fig. (5), for different Richardson numbers, the distributions of Nusselt numbers along the perimeter of the upstream and downstream cylinders are provided. For $L_{cc}/d = 3$, $Re = 100$, $Re = 200$ and $Re = 500$, for different Richardson numbers, the local distributions of the Nusselt number along the perimeter of the upstream and downstream cylinders are provided. For $L_{cc}/d = 3$, the heat transfer characteristics between two closely spaced cylinders differ significantly. While the local Nusselt number profile of the upstream cylinder resembles that of an isolated cylinder, the downstream cylinder exhibits distinct behavior. This discrepancy arises due to the strong connection between heat transfer and fluid flow. Specifically, we observed localized regions of minimal heat transfer at the front and back stagnation points of the downstream cylinder. These points experience relatively low flow velocities, which impact the heat transfer process.

(a)　　　　　　　　　　　　**(b)**
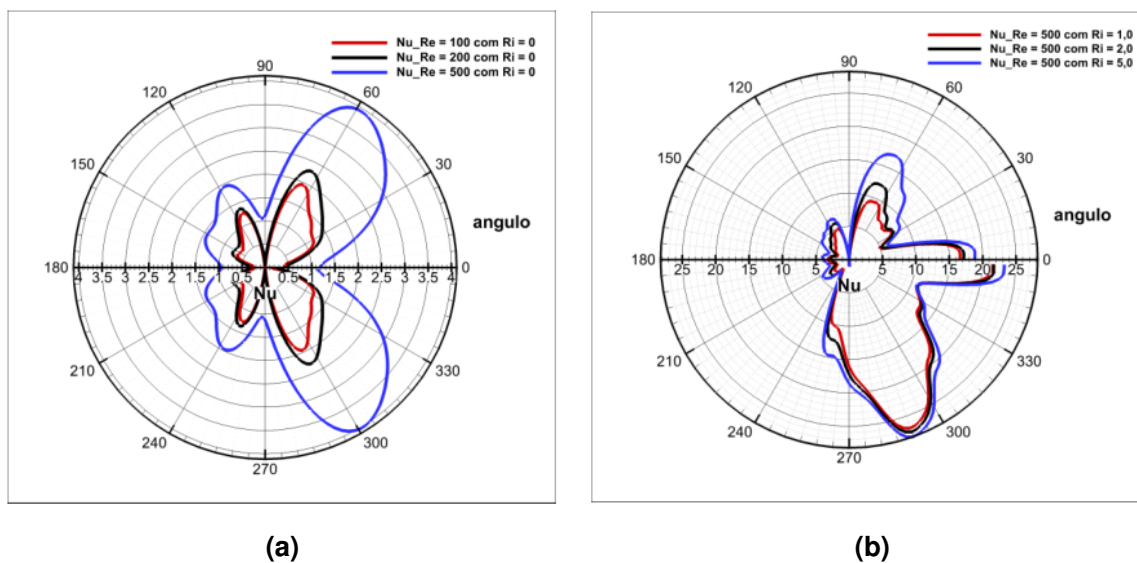
Fig. 5. Local variation of the Nusselt number to the same dimensionless instant. (a) - $Re = 100$, $Re200$ and $Re = 500$ for $Ri = 0$ (forced convection) and (b) - $Re = 500$ for $Ri = 1.0$, $Ri = 2.0$ and $Ri = 5.0$ (natural convection).

Thus, in Fig. (5-(a)), the maximum heat-transfer from the downstream cylinder is exhibited with a double protuberance occuring in $\theta \approx 57°$ and $\theta \approx 265°$ from the cylinder wall, where thermal layers (also known as thermal plumes) and hydrodynamics becomes thinner. The formation of vortices in the downstream region of the cylinder coincides with the oscillation of the average Nusselt number from large amplitude to low amplitude during a vortex release period for $L_{cc}/d = 3$ and $Re = 500$ for different values of Ri as see in Fig. (5-(b)).

It is important to note that although the Nusselt's local distribution of the downstream

cylinder resembles that of the upstream cylinder, typified as a large protuberance, its magnitude is smaller than of the upstream cylinder, indicating smaller heat-to-cylinder convection to downstream.

6 Conclusions

In this work, a boundary condition-enforced immersed boundary method is developed for simulations of heat and mass transfer problems. The effect of thermal boundaries in the flow and temperature fields is considered through the velocity and temperature corrections. The temperature correction is evaluated implicit in such a way that the temperature at the immersed boundary, interpolated from the corrected temperature field, satisfies the physical boundary conditions.

For the momentum transfer between the immersed body and the surrounding fluid, the additional momentum forcing obtained by using the forcing term is added to the fluid-body equations. To model the onset of turbulence, the Spalart-Allmaras model is used. This model uses URANS concept, with only one transport equation for turbulence viscosity, being calibrated in pressure gradient layers. A computational code was developed to implement the mentioned methodology and analyze the combined heat-transfer phenomena and the onset of turbulence for thermofluid dynamics interactions around complex isothermal geometries. The agreement of the results with the available data in the literature validates the numerical method.

Abbreviations
IBM = Immersed Boundary Method
l.h.s. = left hand side
r.h.s. = right hand side
RANS = Reynolds Averaged Navier-Stokes

Disclosure statement. The authors declare no conflict of interest in the writing of the manuscript, or in the decision to publish the results.

ORCID
Rômulo D. C. Santos ⓘ https://orcid.org/0000-0002-9482-1998
Quétila G. Silva ⓘ https://orcid.org/0009-0000-5928-507X
Samia R. L. Tananta ⓘ https://orcid.org/0009-0004-6842-5221

References

1. Peskin, C. S. (1972). Flow Patterns Around Heart Valves: A Numerical Method. *J. Comput. Phys.*, **10**(2), 252–271. https://doi.org/10.1016/0021-9991(72)90065-4
2. Peskin, C. S. (1977). Numerical Analysis of Blood Flow in the Heart. *J. Comput. Phys.*, **25**, 220–252.
3. Park, S. G., Chang, C. B., Kim, B. and Sung, H. J. (2017). Simulation of Fluid-Flexible Body Interaction with Heat Transfer. *Int. J. Heat Mass Transfer*, **110**, 20–33. https://doi.org/10.1016/j.ijheatmasstransfer.2017.03.012

4. Ashrafizadeh, A. and Hosseinjani, A. A. (2017). A Phenomenological Study on the Convection Heat Transfer around Two Enclosed Rotating Cylinders via an Immersed Boundary Method. *Int. J. Heat Mass Transfer*, **107**, 667–685. https://doi.org/10.1016/j.ijheatmasstransfer.2016.11.078

5. Mittal, R. and Iaccarino, G. (2005). Immersed Boundary Method. *Annu. Rev. Fluid Mech.*, **37**, 239–261. https://doi.org/10.1146/annurev.fluid.37.061903.175743

6. Lai, M. C., & Peskin, C. S. (2000). An Immersed Boundary Method with Formal Second-Order Accuracy and Reduced Numerical Viscosity. *J. Comput. Phys.*, **160**(2), 705–719. https://doi.org/10.1006/jcph.2000.6483

7. Goldstein, D., Handler, R., & Sirovich, L. (1993). Modeling a No-slip Flow Boundary with an External Force Field. *J. Comput. Phys.*, **105**(2), 354–366. https://doi.org/10.1006/jcph.1993.1081

8. Yang, Q. and Cao, S. (2013). Numerical Simulation of Flow around Bluff Bodies Based on Virtual Boundary Method. The 8th Asia–Pacific Conference on Wind Engineering, Chennai, pp. 10-14, 582-591. https://doi.org/10.3850/978-981-07-8012-8_154

9. Mohd-Yusof, J. (1997). For simulations of flow in complex geometries. *Annual Research Briefs*, 317.

10. Ye, T., Mittal, R., Udaykumar, H. S., & Shyy, W. (1999). An Accurate Cartesian Grid Method for Viscous Incompressible Flows with Complex Immersed Boundaries. *J. Comput. Phys.*, **156**(2), 209–240. https://doi.org/10.1006/jcph.1999.6356

11. Santos, R. D., Gama, S. M., & Camacho, R. G. (2018). Two-Dimensional Simulation of the Navier-Stokes Equations for Laminar and Turbulent Flow around a Heated Square Cylinder with Forced Convection. *Applied Mathematics*, **9**(03), 291–312. https://doi.org/10.4236/am.2018.93023

12. Silva, A. L. E., Silveira-Neto, A. and Damasceno, J. J. R. (2003). Numerical Simulation of Two-Dimensional Flows over a Circular Cylinder using the Immersed Boundary Method. *J. Comput. Phys.*, **189**, 351–370. https://doi.org/10.1016/s0021-9991(03)00214-6

13. Chorin A. J. (1968). Numerical Solution of the Navier-Stokes Equations. *Mathematics of computation*;**22**(104):745–762. https://doi.org/10.1090/s0025-5718-1968-0242392-2

14. Chatterjee, D. (2010). Mixed Convection Heat Transfer from Tandem Square Cylinder in Vertical Channel at Low Reynolds Numbers. *Numerical Heat Transfer, Part A: Applications*, **58**(9), 740–755. https://doi.org/10.1080/10407782.2010.516703

15. Singh, S., Panigrahi, P. & Muralidhar, K. (2007). Effect of Bouyancy on the Wakes of Circular and Square Cylinders: A Schlieren-Interferometric Study. *Experiments in fluids*, **43**(1):101–123. https://doi.org/10.1007/s00348-007-0329-8

16. Moulay, M. A., Belkady, M., Aounallah, A. *et.al.* (2017). Effect of Opposing Bouyancy on Two-dimensional Laminar Flow and Heat Transfer Across a Confined Circular Cylinder. *Mechanics*, **23**(6):859–865. https://doi.org/10.5755/j01.mech.23.6.17291

17. Anjaiah, N., Dhiman, A. & Chhabra, R. (2006). Mixed Convection Heat Transfer from a Square Cylinder to Power-Law Fluids in Cross-Flow. In *AMSE 2006 2nd Joint US-Europen Fluids Engineering Summer Meeting Collocated with the 14^{t}h International Conference on Nuclear Engineering*, pp. 1435–1444. American Society of Mechanical Engineers. https://doi.org/10.1115/fedsm2006-98072

18. Dhiman, A., Anjaiah, N., Chhabra, R. & Eswaran, V. (2007). Mixed Convection from Heated Square Cylinder to Newtonian and Power-Fluids. *Journal of Fluids Engineering*, **129**(4):506-513. https://doi.org/10.1115/1.2436586

19. Sharma, N., Dhiman, A. K., & Kumar, S. (2012). Mixed Convection Flow and Heat Transfer Across a Square Cylinder Under the Influence of Aiding Buoyancy at Low Reynolds Numbers. *Int. J. Heat Mass Transfer*, **55**(9-10), 2601–2614. https://doi.org/10.1016/j.ijheatmasstransfer.2011.12.034

20. Breuer, M., Bernsdorf, J., Zeiser, T. & Durst. F. (2000). Accurate Computations of

the Laminar Flow Past a Square Cylinder Based on Two Different Methods: Lattice-Boltzmann and Finite Volume. *International Journal of Heat and Fluid Flow*, **21**(2):186–196. https://doi.org/10.1016/s0142-727x(99)00081-8

21. Kim, J., Kim, D. & Cho, H. (2001). An Immersed-Boundary Finite-Volume Method for Simulations of Flow in Complex Geometries. *J. Comput. Phys.*, **171**(1):132–150. https://doi.org/10.1006/jcph.2001.6778

22. Kim, J. & Cho, H. (2004). An Immersed-Boundary Finite-Volume Method for Simulation of Heat Transfer in Complex Geometries. *KSME International Journal*, **18**(6):1026–1035. https://doi.org/10.1007/bf02990875

23. Perumal, D. A., Kumar, G. V., & Dass, A. K. (2012). Numerical Simulation of Viscous Flow over a Square Cylinder Using Lattice Boltzmann Method. *ISRN Mathematical Physics*,2012. https://doi.org/10.5402/2012/630801

24. Sharma, A. (2003). Numerical Investigation of Unconfined and Channel-Confined Flow Across a Square Cylinder with Forced and Mixed Convection Heat Transfer. *Ph.D. thesis*, Indian Institute of Technology Kanpur, India.

25. Sharma, A. & Eswaran, V. (2004). Effect of Aiding and Opposing Buoyancy on the Heat and Fluid Flow Across a Square Cylinder at $Re = 100$. *Numerical Heat Transfer, Part A: Applications*, **45**(6):601–624. https://doi.org/10.1080/10407780490277798

26. Sohankar, A. & Etminan, A. (2009). Forced-Convection Heat Transfer from Tandem Square Cylinders in Cross Flow at low Reynolds Numbers. *International Journal for Numerical Methods in Fluids*, **60**(7):733–751. https://doi.org/10.1002/fld.1909

27. Yen, S., San, K., & Chuang, T. (2008). Interactions of Tandem Square Cylinders at Low Reynolds Numbers. *Experimental Thermal and Fluid Science*, **32**(4):927–938. https://doi.org/10.1016/j.expthermflusci.2007.07.001

28. Smagorinsky, J. (1963) General Circulation Experiments with the Primitive Equations: I. The Basic Experiment. *Monthly Weather Review*, **91**, 99–164. https://doi.org/10.1175/1520-0493(1963)091%3C0099:gcewtp%3E2.3.co;2

29. Spalart, P. & Allmaras, S. (1992). A One-Equation Turbulence Model for Aerodynamics Flows. *Recherce Aeropatiale*, No. 1, 5–21.

30. Mahir, N. & Altaç, Z.(2008). Numerical Investigation of Convective Heat Transfer in Unteady Flow Past Two Cylinders in Tandem Arragements. *International Journal of Heat and Fluid Flow*, **29**(5):1309–1318. https://doi.org/10.1016/j.ijheatfluidflow.2008.05.001

31. Sohankar, A., Norberg, C. & Davidson, L. (1999). Simulation of Three-Dimensional Flow Around a Square Cylinder at Moderate Reynolds Numbers. *Physics of Fluids*, **11**(2): 288–306. https://doi.org/10.1063/1.869879

32. Santos, R. D. C. d. (2014). Análise Bidimensional Termo-Fluido Dinâmica de Cilindros Rotativos com o Método da Fronteira Imersa/Modelo Físico Virtual. *Master's thesis*. Universidade Federal de Itajubá - Minas Gerais, Brazil.

33. Laidoudi, H. & Bouzit, M. (2016). Mixed Convection in Poiseuille Fluid from an Asymmetrically Confined Heated Circular Cylinder. *Thermal Science*, (00): 172–172.

34. Zdravkovich, M. (1985). Flow Induced Oscillations of Two Interfering Circular Cylinders. *Journal of Sound and Vibrations*, **101**(4): 511–521. https://doi.org/10.1016/s0022-460x(85)80068-7